2D CTAB-MoSe$_2$ Nanosheets and 0D MoSe$_2$ Quantum Dots: Facile Top-Down Preparations and Their Peroxidase-Like Catalytic Activity for Colorimetric Detection of Hydrogen Peroxide

Da-Ren Hang [1,2,*,†] , **Ya-Qi Pan** [1,†], **Krishna Hari Sharma** [1], **Mitch M. C. Chou** [1,2],
Sk Emdadul Islam [3] , **Hui-Fen Wu** [4] **and Chi-Te Liang** [3,*]

[1] Department of Materials and Optoelectronic Science, National Sun Yat-sen University,
   Kaohsiung 80424, Taiwan; zxcasd010379@gmail.com (Y.-Q.P.); krishnaharisharma.27@gmail.com (K.H.S.);
   mitch@faculty.nsysu.edu.tw (M.M.C.C.)
[2] Center of Crystal Research, National Sun Yat-sen University, Kaohsiung 80424, Taiwan
[3] Department of Physics, National Taiwan University, Taipei 10617, Taiwan; sk.emdadul87@gmail.com
[4] Department of Chemistry, National Sun Yat-sen University, Kaohsiung 80424, Taiwan;
   hwu@faculty.nsysu.edu.tw
*   Correspondence: drhang@faculty.nsysu.edu.tw (D.-R.H.); ctliang@phys.ntu.edu.tw (C.-T.L.);
   Tel.: +886-7-5252000 (ext. #4066) (D.-R.H.); +886-2-33665129 (C.-T.L.)
†   These authors contributed equally to this work.

check for updates

Abstract: We report the facile and economic preparation of two-dimensional (2D) and 0D MoSe$_2$ nanostructures based on systematic and non-toxic top-down strategies. We demonstrate the intrinsic peroxidase-like activity of these MoSe$_2$ nanostructures. The catalytic processes begin with facilitated decomposition of H$_2$O$_2$ by using MoSe$_2$ nanostructures as peroxidase mimetics. In turn, a large amount of generated radicals oxidizes 3,3,5,5-tetramethylbenzidine (TMB) to produce a visible color reaction. The enzymatic kinetics of our MoSe$_2$ nanostructures complies with typical Michaelis–Menten theory. Catalytic kinetics study reveals a ping–pong mechanism. Moreover, the primary radical responsible for the oxidation of TMB was identified to be $\dot{O}_2{}^-$ by active species-trapping experiments. Based on the peroxidase mimicking property, we developed a new colorimetric method for H$_2$O$_2$ detection by using 2D and 0D MoSe$_2$ nanostructures. It is shown that the colorimetric sensing capability of our MoSe$_2$ catalysts is comparable to other 2D materials-based colorimetric platforms. For instance, the linear range of H$_2$O$_2$ detection is between 10 and 250 μM by using 2D functionalized MoSe$_2$ nanosheets as an artificial enzyme. Our work develops a systematic approach to use 2D materials to construct novel enzyme-free mimetic for a visual assay of H$_2$O$_2$, which has promising prospects in medical diagnosis and food security monitoring.

Keywords: MoSe$_2$ quantum dots; peroxidase-like activity; hydrogen peroxide; few-layer MoSe$_2$ nanosheets; colorimetric detection

1. Introduction

The development of convenient and sensitive detection of hydrogen peroxide (H$_2$O$_2$) is in high demand in the fields of food security, environmental monitoring and biochemical analysis. H$_2$O$_2$, produced from the incomplete reduction of O$_2$, can be found as a byproduct in diverse biological processes. Higher amounts than normal of cellular H$_2$O$_2$ have been linked to the risk of a few diseases including Parkinson's disease and cancer development [1,2]. Thus, it is of practical importance to analyze and detect H$_2$O$_2$ by a simple, sensitive and economic method. So far, various

techniques for H_2O_2 determination have been explored, such as fluorometry [3,4], cellular imaging [5], electrochemistry [6,7], and the colorimetric method [8,9]. Among these approaches, the colorimetric method has drawn a lot of attention due to its convenient operation, visibility, facile miniaturization, and low cost [10,11]. In this respect, natural enzymes were extensively used for the detection of H_2O_2 due to its catalysis capability under mild conditions. Nevertheless, these conventional enzymes usually suffer from the disadvantages of low stability against harsh conditions and high expenditures for preparation and purification. Consequently, researchers actively sought artificial enzyme-mimic materials without these shortcomings. Nanomaterials are currently regarded as a rich source to synthesize desired alternative mimic enzymes with the benefits of low cost, plentiful raw materials, and ease in purification and storage. Many nanomaterials with intrinsic enzyme-mimetic activity analogous to that of natural enzymes were fabricated, such as metal organic frameworks [12], Pt nanoclusters [13], silver nanoparticles [14], and gold nanoparticles [15]. Although enormous progress has been made, the discovery and development of novel promising artificial peroxidase mimics is still in urgent need.

With the persistent advancement of nanotechnology and materials science, two-dimensional (2D) nanomaterials beyond graphene have received much attention because of many fascinating chemical and physical properties. The transition metal dichalcogenides (TMDs), a family of layered compound materials consisting of 2D sheets weakly bound by van der Waals interactions, is the most renowned group of emerging 2D materials. They have shown huge promise in a wide range of applications. In particular, TMD nanostructures have shown good potential in biomedical applications due to their large surface area, low cytotoxicity, and higher structural rigidity than other 2D nanomaterials. For instance, it was found that TMDs exhibited lower cytotoxicity than typical graphene and its analogues [16]. As for structural rigidity, commonly used graphene and hexagonal boron-nitride have relatively low flexural rigidity around 3.5 eV $Å^2$/atom. On the other hand, these values for MoS_2 and WS_2 are 27 eV $Å^2$/atom and 30 eV $Å^2$/atom, respectively [17]. These properties should make 2D TMDs appropriate for biomedical applications. Finally, TMDs can remain stable in liquid due to the lack of dangling bonds on the surface, which supports their use in biomedical applications.

Molybdenum disulfide (MoS_2), the most prominent member of the TMD family, possesses distinctive properties and has found diverse successful applications in electronics [18], energy devices [19], photocatalysis [20], and sensors [21,22]. In particular, the peroxidase-like catalytic ability of a few MoS_2 nanostructures has been shown by researchers [23,24]. While a large amount of investigations is devoted to MoS_2, considerably less attention has been devoted to molybdenum diselenide ($MoSe_2$) [25]. 2H-$MoSe_2$, also with a graphene-like lamellar structure, is a semiconductor whose bandgap energy increases from ~1.1 eV in bulk to ~1.55 eV in ultrathin form with atomic thickness. In a previous comparative study, Gholamvand and coworkers concluded that $MoSe_2$ is the most effective electrocatalyst among TMDs [26]. Recent studies also showed that few-layered $MoSe_2$ nanosheets (NSs) could be a promising candidate with peroxidase-like activity and good biocompatibility [27,28]. Moreover, inspired by the fact that selenium-containing enzymes are generally prevalent in the biosphere and their active sites usually involve selenium, we thus turned our attention to the investigation of nanoscale $MoSe_2$ in this respect. Even though $MoSe_2$ is expected to function as efficient peroxidase mimetics for colorimetric detection, so far little progress has been made in this respect. Its extended topics, such as surface modification and variation in dimensionality, were rarely studied for use in colorimetric detection. Here, we intend to fill the gap along this exploration. For instance, TMD in quantum dot (QD) form deserves more investigation because their pronounced quantum confinement effects (QCE) and edge effects further aid applications in catalysts and sensing [29,30]. Significant enhancement in photoluminescence (PL) quantum efficiency by QCE is favorable to develop a sensor by optical means [31,32]. Moreover, a few optical properties in the strong coupling regime for semiconductor QDs and nanostructures could be implemented to strengthen the functionality of biosensors [33–35].

Liquid-phase synthesis routes are suitable to produce TMD nanostructures in large quantity at low cost. In general, solution-based synthesis approaches can be divided into "top-down" methods and "bottom-up" methods. For bottom-up wet-chemical synthesis methods, specific precursors are needed and a high-temperature and high-pressure environment is required. Among top-down approaches, liquid phase exfoliation (LPE) is a powerful technique to efficiently exfoliate various types of layered crystals into few-layer nanosheets or even QDs [36,37]. The basic protocol of LPE technique is very general and only parent crystal is needed instead of the need for specific precursors in bottom-up chemical methods.

In this paper, we prepared two types of low-dimensional $MoSe_2$ nanostructures based on top-down techniques. In the first case, LPE-derived 2D $MoSe_2$ nanosheets were functionalized with cetyltrimethyl ammonium bromide (CTAB). It is expected that the CTAB surfactant could aid exfoliation efficiency and prevent 2D nanosheets from restacking or agglomeration [38]. Secondly, 0D $MoSe_2$ QDs were obtained based on top-down exfoliation approaches. For usual 0D TMD QDs derived from LPE, longer ultrasonication time and higher power were typically adopted, which could easily deform the microstructure and result in higher density of surface traps states. As surface-to-volume ratio is rather large for QDs, these deep trap states pose negative impact to many applications. In our work, a novel and efficient ultrasonication-assisted solvothermal exfoliation technique is firstly introduced for preparing small size and high-quality $MoSe_2$ QDs. In the initial probe-assistant ultrasonication exfoliation phase, $MoSe_2$ bulk is broken into nanosheets or nanoparticles by the acoustic cavitation effect. The sonication time is kept short in this stage. Next, the solvothermal treatment with a polar solvent continuously weakens the van der Waals forces of thinned $MoSe_2$ and break it up into small 0D QDs. We show that our CTAB-modified $MoSe_2$ NSs and 0D $MoSe_2$ QDs are able to efficiently catalyze the oxidation of 3,3,5,5-tetramethylbenzidine (TMB) in the presence of H_2O_2 to produce a colored product. On this basis, we have successfully demonstrated novel platforms for colorimetric detection of H_2O_2. It is found that the sensing capability of our $MoSe_2$ systems is comparable to those of published 2D materials-based platforms. As far as we know, it is the first time the potential of CTAB-functionalized $MoSe_2$ nanosheets and 0D $MoSe_2$ QDs have been explored for colorimetric detection of H_2O_2. Toxic and high boiling point solvents were not used in our synthesis methods thus our protocols also provide a non-toxic and systematic way to fabricate new 2D nanomaterials for construction of novel colorimetric sensors and for use in extended applications.

2. Materials and Methods

2.1. Materials and Reagents

$MoSe_2$ powder (99.9%), 3,3,5,5-tetramethylbenzidine (TMB), and isopropanol were purchased from Sigma-Aldrich (St. Louis, MO, USA). Cetyltrimethyl ammonium bromide (CTAB) was purchased from Millipore (Burlington, MA, USA). Acetic acid, sodium acetate anhydrous, hydrochloric acid, and hydrogen peroxide (35%) were obtained from Alfa Aesar (Tewksbury, MA, USA). These chemicals were of analytical purity and were used as received. Deionized water (DI water) was used as a solvent throughout.

2.2. Methods

2.2.1. Preparation of Surfactant Modified Two-Dimensional (2D) $MoSe_2$ Nanosheets (NSs)

The few-layer CTAB-$MoSe_2$ NSs synthesis protocol is based on the grinding-assisted liquid phase exfoliation approach [37]. The synthesis protocol of 2D CTAB-$MoSe_2$ NSs is illustrated in Figure 1a. First, 100 mg of $MoSe_2$ powder and 50 mg of CTAB were ground for 30 min. The mixture was subsequently dispersed in 20 mL of DI water and stirred for 1 h at 90 °C in a beaker. The solution was probe sonicated for 3 h with a horn sonic tip (Qsonica CL-334) at a power output of 125 W in a water-cooled bath at 20 °C. Residual sediment and thick flakes were further removed by centrifugation

at 4000 rpm for 20 min. The upper portion of the supernatant was taken for the next centrifugation for 20 min at the speed of 9000 rpm. The upper portion of the resultant supernatant was transferred to a refrigerator at 4 °C for storage. Finally, the 2D CTAB-MoSe$_2$ NS product was collected by another centrifugation at the speed of 9000 rpm.
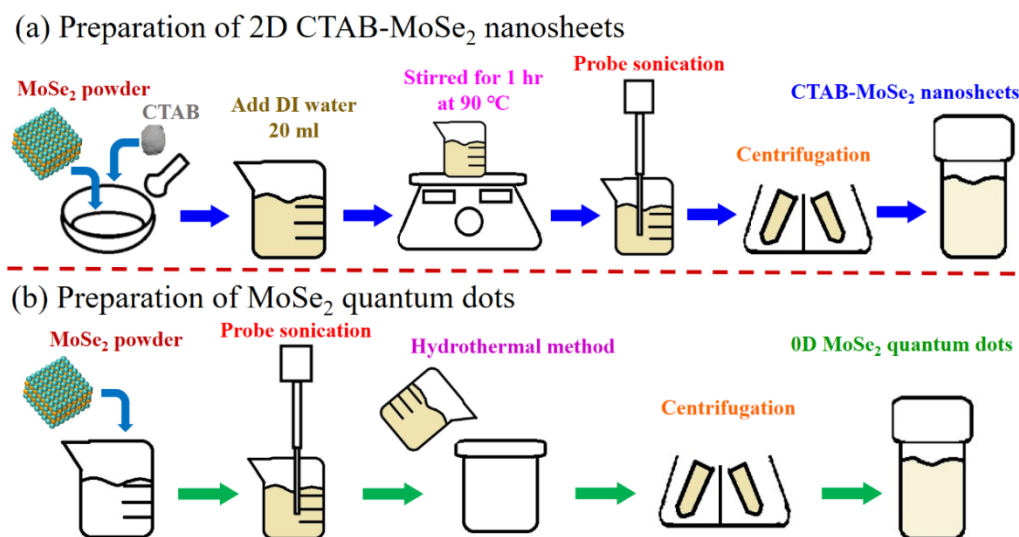

Figure 1. The schematic illustrations for the preparations of (**a**) two-dimensional (2D) cetyltrimethyl ammonium bromide (CTAB)-MoSe$_2$ nanosheets and (**b**) 0D MoSe$_2$ quantum dots (QDs).

2.2.2. Preparation of 0D MoSe$_2$ QDs

The 0D MoSe$_2$ QDs were obtained according to the ultrasonication-assisted solvothermal exfoliation technique. Figure 1b depicts the synthesis procedure of 0D MoSe$_2$ QDs. Typically, 100 mg of MoSe$_2$ powder was dispersed in 60 mL of 50 vol% **Isopropyl alcohol** (IPA)/DI water mixture in a beaker. Then, the solution was probe sonicated for 1 h with a horn sonic tip (Qsonica CL-334) at a power output of 150 W in a water-cooled bath at 20 °C. Afterward, the resultant dispersions was further transferred to a 60 mL Teflon-lined autoclave and reacted at 200 °C for 24 h. After the autoclave cooled naturally, the supernatant containing MoSe$_2$ QDs was centrifuged for 30 min at the speed of 9000 rpm. After that, the upper portion of the supernatant was collected for second centrifugation for 15 min with the same rotation speed. Finally, the MoSe$_2$ QD product was collected and then stored in a refrigerator at 4 °C for use.

2.3. Characterization

Transmission electron microscopy (TEM) images and high-resolution TEM (HRTEM) images were taken by using a JEOL-3010 transmission electron microscope at an accelerating voltage of 200 kV (Tokyo, Japan). The elemental composition and bonding configuration analysis were carried out by an ultrahigh vacuum JEOL JPS-9010 X-ray photoelectron spectrometer (XPS) equipped with a multi-channel detector. The detected binding energies were calibrated to the C1 s peak at 284.8 eV of the surface adventitious carbon. The ultraviolet–visible (UV–vis) spectra were recorded with a Jasco V-730 spectrophotometer (USA) with a standard 10-mm path length quartz cuvette (Easton, MD, USA). The photoluminescence spectra were measured using a Hitachi F-4500 florescence spectrophotometer connected to a 150 W Xenon lamp as the excitation source. The Raman spectra were recorded in ambient conditions using a confocal microscope linked to a Horiba iHR320 spectrometer (Piscataway, NJ, USA) [39].

2.4. Peroxidase-Mimetic Activity of MoSe$_2$ Quantum Dots (QDs) and 2D Cetyltrimethyl Ammonium Bromide (CTAB)-MoSe$_2$ NSs

To evaluate the catalytic peroxidase-like properties, a blue product was generated by the peroxidase substrate TMB in the presence of H$_2$O$_2$. In a typical experiment, 600 µL 0.1 mg/mL MoSe$_2$ catalyst was incubated with 500 µL acetate buffer solution (0.1 M, pH 3.6), 200 µL H$_2$O$_2$ (10 mM), 200 µL TMB (5 mM) and 60 µL H$_2$O at room temperature for 15 min. Then, the absorbance of the mixture was measured by a Jasco V-730 UV-visible spectrophotometer (Easton, MD, USA). For H$_2$O$_2$ detection, different contents of H$_2$O$_2$ were incubated with 600 µL 0.1 mg/mL MoSe$_2$ catalyst, 500 µL acetate buffer solution (0.1 M, pH 3.6) and 200 µL TMB (5 mM) at room temperature for 15 min, and then the absorbance at 652 nm was recorded.

3. Results and Discussion

3.1. Structural Studies

The microstructure of the resultant MoSe$_2$ nanomaterials is characterized by transmission electron microscopy (TEM). As shown in Figure 2a, the as-obtained MoSe$_2$ QDs reveal a spherical shape without noticeable aggregation, indicating the successful formation of highly dispersive QDs. The statistical analysis of particle size distribution was conducted by counting 700 QD profiles measured by TEM. The outcome is displayed by the histogram in Figure 2b along with its calculated Gaussian fitting curve. The average size of the 0D QDs was determined to be 4.5 nm and up to 80% QDs have their diameters in the narrow range from 3 to 6 nm. A high-resolution TEM (HRTEM) image of a single MoSe$_2$ QD in the inset of Figure 2a reveals that the lattice spacing of the synthesized QD was 0.23 nm, which coincides with the (103) plane of hexagonal MoSe$_2$ [40].
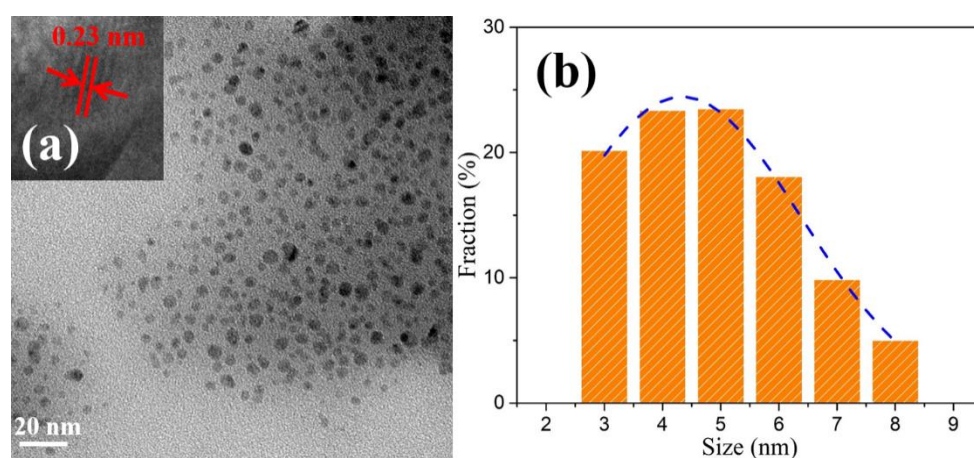

Figure 2. (**a**) Transmission electron microscope (TEM) image of synthesized MoSe$_2$ QDs. The inset shows representative high-resolution TEM (HRTEM) image of the MoSe$_2$ QD. (**b**) Statistical analysis of the size of MoSe$_2$ QDs measured by TEM and its Gaussian fitting curve.

Next, Figure 3a shows the representative TEM image of the as-prepared 2D CTAB-MoSe$_2$ nanosheet, in which a sheet-like structure can be found. The HRTEM image in the inset of Figure 3a resolves lattice fringes with lattice spacing of 0.28 nm, which is in agreement with the (100) plane of 2H-MoSe$_2$. As shown in Figure 3b, the selected-area electron diffraction (SAED) pattern again verifies the diffraction pattern from the 2H-MoSe$_2$ crystal and demonstrates the good crystallinity of the exfoliated nanosheets. Atomic force microscopy (AFM) measurement was adopted to further confirm the 2D nature of CTAB-MoSe$_2$ nanosheets. A representative AFM image is shown in Figure 3c and the height profile along the black line was measured. It was found that the nanosheet thickness ranges from 4.2 to 4.7 nm, which confirms the 2D few-layered structure.
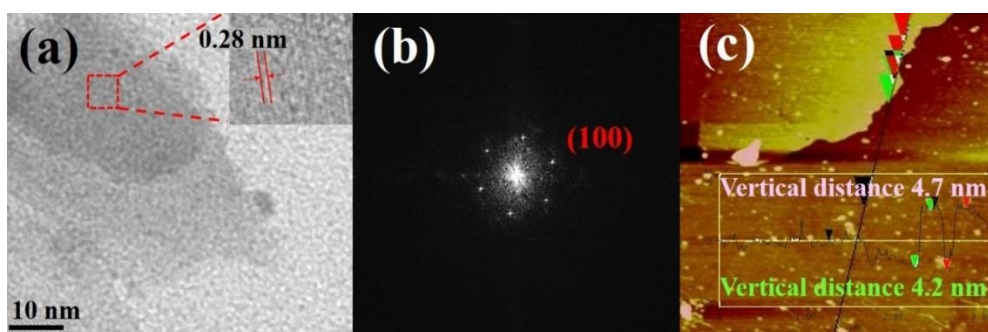
Figure 3. (**a**) TEM image of 2D CTAB-MoSe$_2$ prepared by liquid phase exfoliation (LPE). The inset shows its HRTEM image (**b**) The selected area electron diffraction pattern (SAED). (**c**) The atomic force microscopy image of as-obtained 2D CTAB-MoSe$_2$ and the corresponding height profile along the black line in the image.

3.2. Surface Elemental and Valence State Analysis

To further shed light on the surface chemical components and oxidation states of our solvothermal-treated MoSe$_2$ QDs, XPS was performed on both pristine bulk MoSe$_2$ powder and MoSe$_2$ QDs. Figure 4a,b show the high-resolution Mo 3d and Se 3d XPS spectra of pristine MoSe$_2$ powder, respectively. The two peaks located at 228.1 eV and 231.2 eV correspond to the Mo 3d$_{5/2}$ and Mo 3d$_{3/2}$ peaks of the Mo^{4+} state in MoSe$_2$, which is in agreement with previous reports [19,41]. Meanwhile, the peak of Se 3d spectrum can be deconvoluted into two components: the binding energy peaks at 53.4 eV and 54.2 eV are characteristic signals of Se^{2-} 3d$_{5/2}$ and Se^{2-} 3d$_{3/2}$, respectively [42]. In this case, a signal from the Mo^{6+} state was not observed, indicating that there is no noticeable oxidation in our pristine material. Next, the high-resolution Mo 3d and Se 3d spectra of MoSe$_2$ QDs are presented in Figure 4c,d, respectively. The deconvolution of Mo 3d spectral region reveals four contributions. The two intense peaks at 227.9 and 231.1 eV belong to the characteristic signals from Mo^{4+} 3d$_{5/2}$ and Mo^{4+} 3d$_{3/2}$, respectively. Furthermore, the other two minor peaks at binding energies of 232.2 and 235.5 eV are ascribed to the Mo(VI) state [37]. This suggests that a small portion of surface Mo^{4+} was oxidized into Mo^{6+} during the imposed reaction [43,44]. As shown in Figure 4d, the two deconvoluted components of the Se 3d doublet appear at 53.5 eV and 54.3 eV, which can be assigned to the Se 3d$_{5/2}$ and Se 3d$_{3/2}$ orbitals of divalent selenide ions (Se^{2-}), respectively. It can be confirmed that the binding energies of Mo^{4+} and Se^{2-} orbitals of our prepared QDs do not deviate noticeably from those of the starting material. It is reasonable as no heterostructure formation or other interaction is involved.
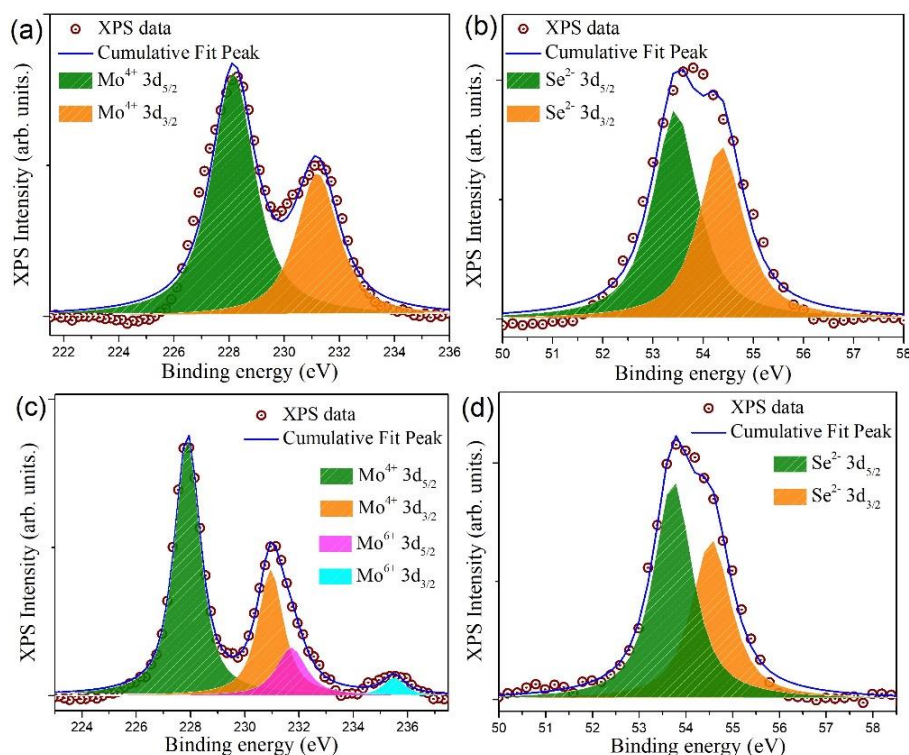
Figure 4. High-resolution X-ray photoelectron spectrometer (XPS) spectra showing the binding energy of (**a**) Mo 3d and (**b**) Se 3d electrons recorded on bulk MoSe$_2$ powder. High-resolution core level spectra corresponding to (**c**) Mo 3d and (**d**) Se 3d electrons for MoSe$_2$ QDs.

3.3. Optical Property Studies

It is known that the dimensionality strongly affects the optical properties of nanoscale semiconductors. The optical absorption spectrum of the resultant CTAB-MoSe$_2$ nanosheets in dispersion is displayed in Figure 5a. The evident absorption peaks at 805 and 695 nm can be easily identified and they are attributed to the characteristic resonances of A and B excitons, respectively [45–47]. Their origin is derived from the transitions between the spin-orbit split valence bands and the lowest conduction band at K and K' points of the Brillouin zone. Moreover, it is worth of noting that the determined energy separation of 244 meV between the A and B excitonic states is consistent with a previous study on the energy splitting of the exciton states in ultrathin MoSe$_2$ nanosheets [48]. Therefore, it provides a quantitative proof of pronounced quantum confinement effect in our exfoliated 2D MoSe$_2$ nanosheets. The facile and conventional way to address the optical band gap is by means of the Tauc plot. The absorption coefficient α of a direct band-gap semiconductor can be related to photon energy $h\upsilon$ by $(\alpha h\upsilon)^2 = A\,(h\upsilon - E_g)$, where A is a constant and E_g is the optical band gap. Figure 5b plots the relationship of $(\alpha h\upsilon)^2$ versus $h\upsilon$, which demonstrates a linear dependence. The calculated optical gap for the apparent absorption is 1.54 eV (805 nm), which exactly coincides with the A excitonic states and highlights the 2D nature of CTAB-MoSe$_2$ nanosheets.
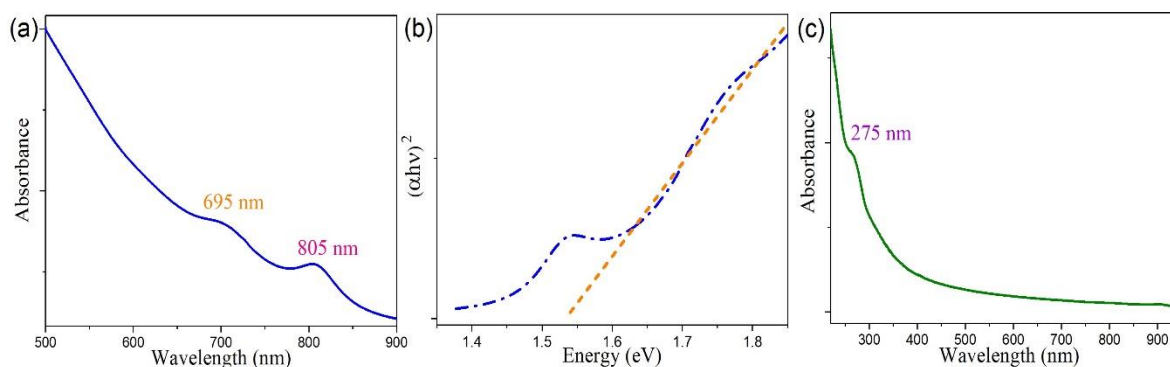
Figure 5. (**a**) Ultraviolet–visible (UV–vis) absorption spectrum of 2D CTAB-MoSe$_2$ nanosheets clearly reveals characteristic excitonic structures. (**b**) The corresponding plot versus (*ahv*)^2 versus *hv* for absorption of 2D CTAB-MoSe$_2$, in which the optical band gap energy can be estimated. (**c**) UV–vis absorption spectrum of MoSe$_2$ QDs. Note the quenching of previous excitonic features in the spectrum.

The optical absorption spectrum of the as-prepared 0D MoSe$_2$ QDs is in sharp contrast with their 2D counterpart, as shown in Figure 5c. Here, the A and B excitonic features in the absorption completely disappeared. Instead, the absorption feature comprised two absorption bands. The prominent band is centered at around 275 nm, which is ascribed to the intrinsic excitonic absorption of the QDs [49,50]. Such a significant blue-shift of the excitonic features directly reflects the dominating quantum confinement effect and is in accordance with previous studies on other TMD QDs [32,51]. Furthermore, there exists another mild absorption band at longer wavelengths. It is wide and centered about 325 nm with a tail extending to ~400 nm, which will be commented upon later.

Photoluminescence (PL) spectroscopy provides a complimentary optical means to probe the electronic structure of semiconductor materials [52,53]. The distinct optical property of TMD QDs is well-suited to be further evidenced by the PL technique. It is easily found that our MoSe$_2$ QDs dispersed in aqueous solution emit strong blue fluorescence under irradiation with a typical UV lamp. It is due to the weak interlayer coupling and enhanced quantum efficiency of MoSe$_2$ QDs, which is another signature of TMD QDs [54]. To gain a comprehensive view of the emission property, the PL spectra of resultant MoSe$_2$ QD dispersion were further taken with different excitation wavelengths, as shown in Figure 6a. It is observed that when the excitation wavelength was increased from 290 to 400 nm, the PL peak position monotonically increased from 390 to 470 nm. Similar excitation-dependent PL behavior has been reported in a few TMD QD reports [32]. In a strong quantum confinement regime, photons with higher energies resonantly excites smaller QDs with wider band gaps, pushing the emission peak to shorter wavelengths. Accordingly, the characteristic excitation-dependent PL behavior derives from the polydispersity of the synthesized QDs. This idiosyncratic variation of PL intensity in response to varying excitation wavelengths can be clearly presented by the 2D color-converted PL contour map as depicted in Figure 6b. We found the strongest emission peaked at 418 nm under an excitation wavelength of 340 nm. This specific wavelength falls coincidentally within the observed absorption band around 325 nm. Thus the close correspondence between the absorption and the emission of the synthesized QDs can be revealed by our optical characterizations.
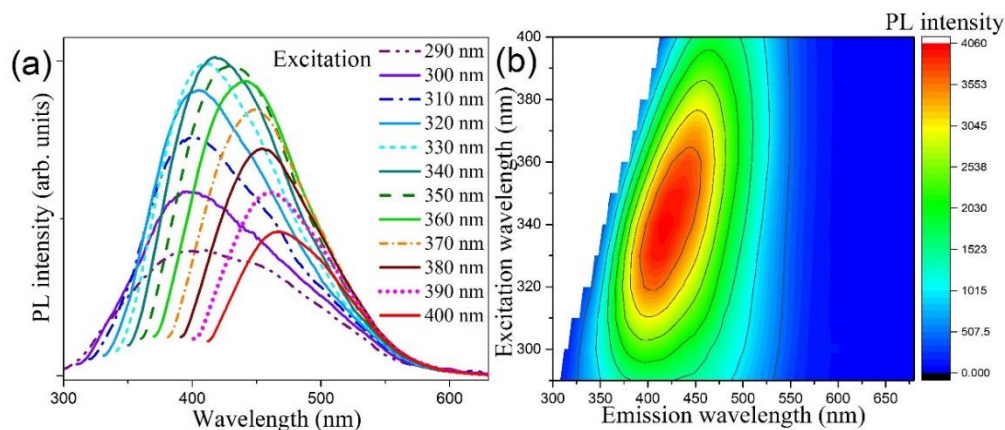
Figure 6. (**a**) Excitation-wavelength dependent photoluminescence (PL) spectra of colloidal $MoSe_2$ QDs at room temperature. (**b**) The 2D contour map acquired from the PL spectra. The characteristic contour is due to the pronounced quantum confinement effect.

Raman spectroscopy was adopted to acquire additional insight into the optical characteristics of 2D CTAB-$MoSe_2$ nanosheets. In general, group theory analysis permits bulk TMDs to have four Raman-active modes. However, only two modes are accessible in typical experimental configuration, namely, out-of-plane A_{1g} and in-plane E^1_{2g} modes. The inset sketch in Figure 7 depicts these two principal Raman-active vibration modes of $MoSe_2$. Figure 7 compares the Raman spectra of both $MoSe_2$ bulk and 2D CTAB-$MoSe_2$ nanosheets. For $MoSe_2$ bulk, the A_{1g} mode is located at 239.4 cm^{-1} while the in-plane E^1_{2g} mode appears at ≈285.5 cm^{-1}, which match nicely with literature values [55]. The A_{1g} mode for CTAB-$MoSe_2$ nanosheets is red-shifted to 237 cm^{-1}, which is attributed to the softening of the vibrational mode [56]. The reduced inter-planar restoring force is another proof for the 2D few-layer structure. In addition, a new peak emerges on the lower-frequency side of the A_{1g} peak. It is ascribed to Davydov splitting of the A_{1g} mode that is accompanied by the suppressed interlayer interaction as reported in TMD nanosheets [57,58]. In contrast, the E^1_{2g} mode for CTAB-$MoSe_2$ shifts to 302 cm^{-1}. The dielectric screening of the long-range Coulomb interaction and the surface effects of TMD materials were proposed to be responsible for this blue-shift [59]. The increased energy splitting between the two allowed Raman peaks is in accord with the 2D nature of our CTAB-$MoSe_2$ [60,61].
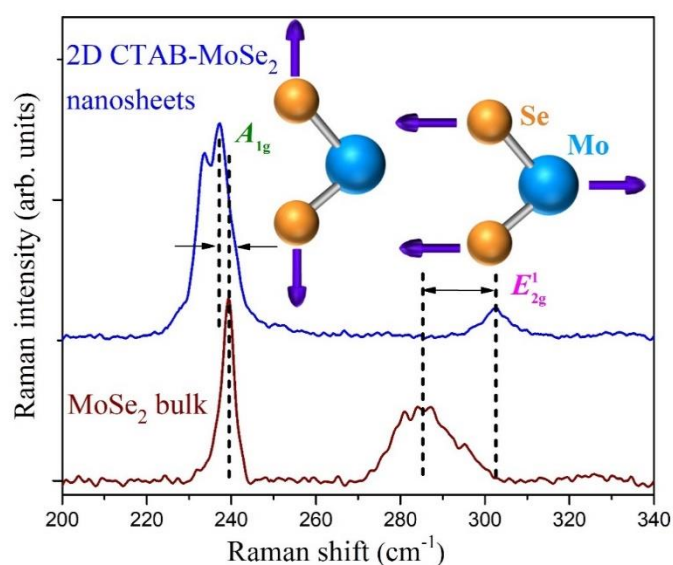

Figure 7. Raman spectra of the source $MoSe_2$ bulk powder (brown line) and as-produced 2D CTAB-$MoSe_2$ nanosheets (blue line). The Raman shifts are denoted by the dashed lines. The inset sketch depicts the atomic displacements of the two vibrational modes leading to the primary Raman peaks.

3.4. Peroxidase-Like Activities and Steady-State Kinetic Assay

We evaluated the peroxidase-like activity of MoSe$_2$ QDs by using the catalytic oxidation of TMB in the presence of H$_2$O$_2$, as shown in Figure 8a. The absorption spectrum of the TMB solution showed it is colorless. When only H$_2$O$_2$ was incubated with TMB, the TMB–H$_2$O$_2$ systems showed rather weak absorbance at 652 nm. Yet as TMB coexisted with H$_2$O$_2$ and the MoSe$_2$ QDs, a prominent absorption peak of the oxidation products of TMB at 652 nm was observed. Moreover, the color contrast of these system is presented in the inset of Figure 8a. It can be seen that the bare TMB and the TMB–H$_2$O$_2$ systems are virtually colorless to the naked eye, while TMB–H$_2$O$_2$–MoSe$_2$ QDs system showed an apparent color variation. Figure 8b display time-dependent absorbance changes at 652 nm of these systems. It clearly shows the absorbance at 652 nm increased as the time increased for TMB–H$_2$O$_2$–MoSe$_2$ QDs system. This means that the prepared MoSe$_2$ QDs possess the peroxidase-like catalysis capability, which effectively catalyze the oxidation of TMB by H$_2$O$_2$. On the contrary, rather insignificant and slow oxidation of TMB by the presence of H$_2$O$_2$ was found for the reference TMB–H$_2$O$_2$ system. Our results thus demonstrated that the MoSe$_2$ QDs can facilitate the oxidation of TMB to oxTMB in the presence of H$_2$O$_2$ to generate observable color changes. An identical result was also found for our 2D CTAB-MoSe$_2$ nanosheets (not shown here).
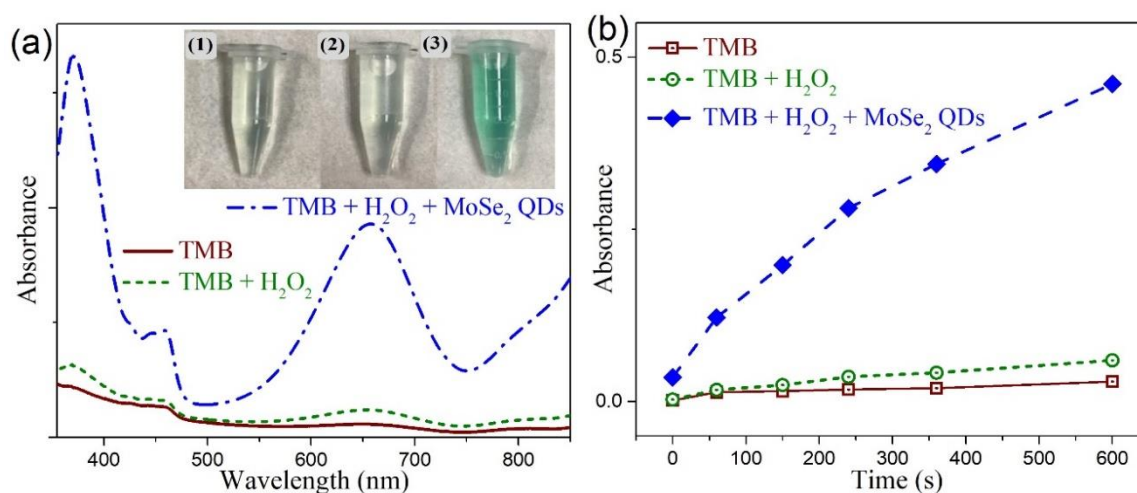

Figure 8. (**a**) UV-visible absorption spectra of (1) 3,3,5,5-tetramethylbenzidine (TMB) solution (brown); (2) TMB–H$_2$O$_2$ system (green); (3) TMB–H$_2$O$_2$–MoSe$_2$ QDs system (blue). Inset: the corresponding photographs of these reaction systems. (**b**) The time-dependent absorbance changes at 652 nm of these systems.

The kinetic parameters of the peroxidase-like reaction were harvested by employing the steady-state kinetics analysis. With H$_2$O$_2$ and TMB as substrates, the measurements were carried out by changing the concentration of one substrate while keeping the other substrate concentration constant. This generates the typical Michaelis–Menten curves, as shown in Figure 9a,b for our MoSe$_2$ QDs. For 2D CTAB-MoSe$_2$ nanosheets, these curves are plotted in Figure 10a,b. The relevant kinetic parameters like the Michaelis–Menten constant (K_m) and the maximal reaction velocity (V_{max}) can be extracted from the Lineweaver–Burk plot according to the relation: $1/v = (K_m/V_{max}) \times (1/[S]) + 1/V_{max}$, where v stands for the initial velocity and $[S]$ signifies the concentration of the substrate [62,63]. Figure 9c,d display the L-B plot for our 0D MoSe$_2$ QDs while Figure 10c,d illustrate the L-B plot for 2D CTAB-MoSe$_2$ nanosheets. The calculated results are listed in Table S1. The K_m value is regarded as an important index that measures the binding affinity of enzyme to the substrates. A smaller value of K_m usually indicates a higher affinity between the enzyme and the substrate. It is found that the K_m value of 2D CTAB-MoSe$_2$ for H$_2$O$_2$ is lower than that of MoSe$_2$ QDs, suggesting a higher affinity of 2D CTAB-MoSe$_2$ to H$_2$O$_2$ than MoSe$_2$ QDs. Meanwhile, the lower K_m value of MoSe$_2$ QDs to TMB represents its higher affinity in this respect. In addition, the parallel slope of the lines in the

double-reciprocal plots of initial velocity versus different concentrations of one substrate reveals a ping-pong mechanism in the catalytic reaction [64–66]. This indicates that both of our $MoSe_2$–based enzymes bound and reacted with the first substrate and the first product was subsequently released before the reaction with the second substrate.
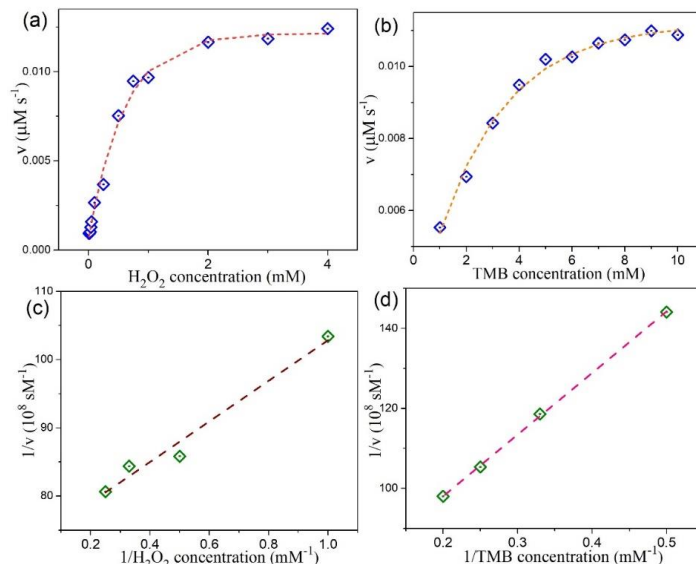

Figure 9. Steady-state kinetic analysis for $MoSe_2$ QDs. The reaction velocity (v) was measured when (**a**) the H_2O_2 concentration was varied while the concentration of TMB was 5 mM and (**b**) the TMB concentration was varied while the concentration of H_2O_2 was 0.75 mM. The corresponding double-reciprocal plots with a fixed concentration of one substrate relative to varying the concentration of the other substrate are displayed in (**c**,**d**).
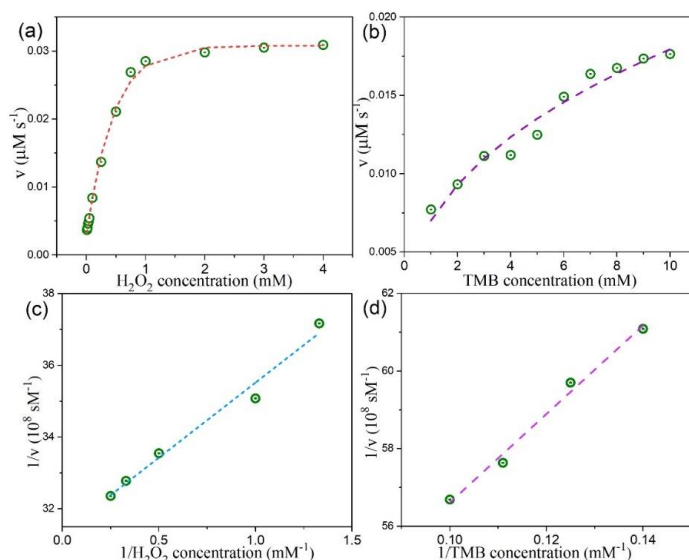

Figure 10. Steady-state kinetic assay of 2D CTAB-$MoSe_2$ nanosheets. (**a**) Varying the concentrations of H_2O_2 while the concentration of TMB was 5 mM. (**b**) Varying the concentrations of TMB while the concentration of H_2O_2 was 0.75 mM. The double-reciprocal plots for the concentration of (**c**) H_2O_2 and (**d**) TMB.

3.5. Actives Species Trapping Tests and Peroxidase-Like Catalytic Mechanism

To confirm the prime species responsible for the peroxidase-mimetic catalytic activities of our artificial $MoSe_2$–based enzymes, scavenger tests were employed. It is known that reaction systems

involving hydrogen peroxide usually abound with reactive radicals such as $\dot{O}H$ and $\dot{O}_2{}^-$. Then IPA and benzoquinone (BQ) were taken to be the scavengers in the reaction system for $\dot{O}H$ and $\dot{O}_2{}^-$ radicals, respectively. Figure 11 shows the results of active species trapping tests of our reaction system. We found that the suppression of characteristic absorption and color fading were not evident with the addition of IPA. On the other hand, significant decrease in absorption and color contrast can be seen when BQ was added. This indicates that $\dot{O}_2{}^-$ radical plays the major role to oxidize TMB to produce a TMB oxide and generate color contrast. Based on our finding and several previous reports [67,68], we propose the peroxidase-like catalytic mechanism of our MoSe$_2$–based enzymes, which is illustrated in Figure 12. In the reaction process, TMB molecules are absorbed on the surface of MoSe$_2$–based nanomaterials and act as the chromogenic electron donors. These molecules transfer their lone-pair electrons to MoSe$_2$ from the amino groups, leading to the enhancement of electron density and mobility on the surface of MoSe$_2$-based catalyst. In turn, it accelerates the electron migration from MoSe$_2$–based catalyst to hydrogen peroxide. The one-electron transfer reaction generate a large amount of $\dot{O}_2{}^-$ radicals that oxidize TMB and form blue-green product. Briefly, the MoSe$_2$-based catalyst promote the electron transfer from TMB to H$_2$O$_2$, resulting in the oxidation of TMB and reduction of hydrogen peroxide. The production of colored oxTMB and water in this system can be expressed by the equation H$_2$O$_2$ + TMB → 2H$_2$O + O$_2$ + oxTMB.
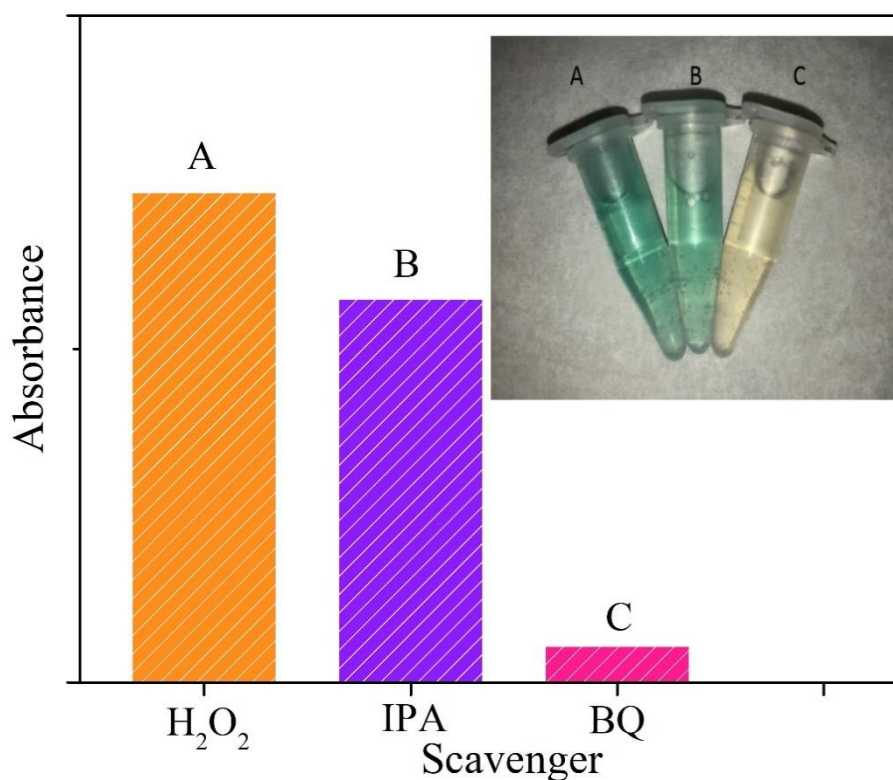

Figure 11. The absorbance at 652 nm of reaction solutions in the absence or presence of scavengers Isopropyl alcohol (IPA) and benzoquinone (BQ). The inset shows the images of color changes for different reaction systems.
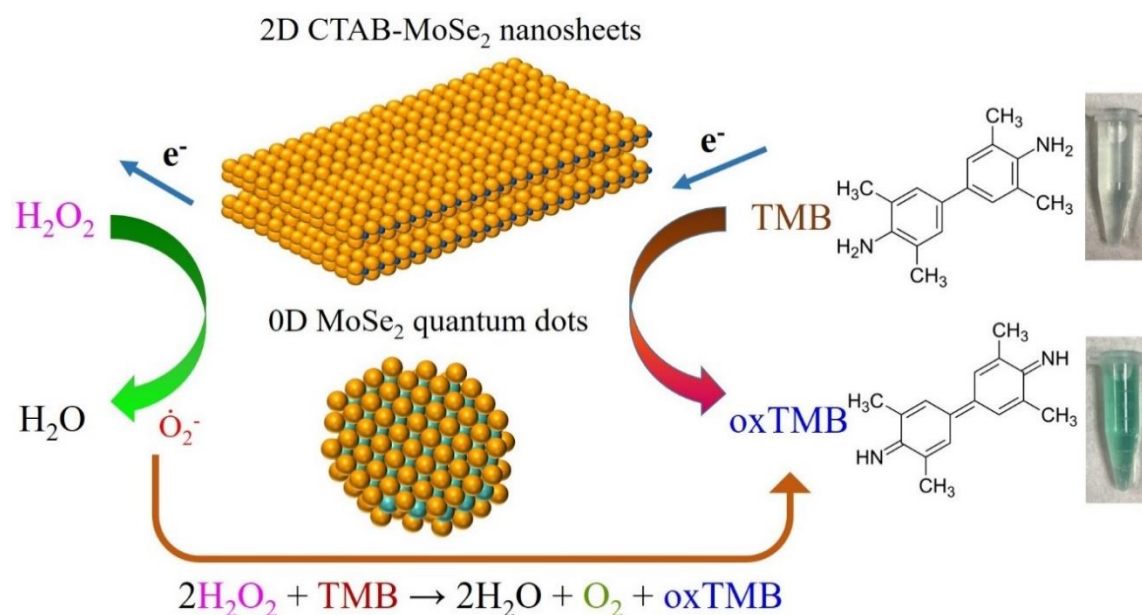
Figure 12. The schematic diagram depicts the mechanism for colorimetric detection of H_2O_2 by using 2D CTAB-MoSe$_2$ NSs and MoSe$_2$ QDs as peroxidase mimetics.

3.6. Colorimetric Detection of H_2O_2 by MoSe$_2$-Based Assay System

In view of the intrinsic peroxidase-like property of as-prepared MoSe$_2$–based catalysts, a colorimetric strategy for the detection of H_2O_2 was established. The absorption spectra of TMB–H_2O_2–MoSe$_2$ QDs system with different H_2O_2 concentration is presented in Figure S1. It can be seen that the characteristic absorption of TMB at 652 nm is dependent on the concentration of H_2O_2 varied from 10 μM to 4 M. Analogous results can be found with our TMB–H_2O_2–2D CTAB-MoSe$_2$ system, as shown in Figure S2. Figures 13a and 14a display the absorbance variations at 652 nm of the oxidized TMB in the presence of H_2O_2 with different concentrations for the TMB–H_2O_2–MoSe$_2$ QDs system and TMB–H_2O_2–2D CTAB-MoSe2 system, respectively. Besides, the corresponding image in response to the change of H_2O_2 is shown in the insets of Figures 13a and 14a, which shows the color variation could be seen by the naked eye. For TMB–H_2O_2–MoSe$_2$ QDs system, the H_2O_2 concentration-response curve has a linear relationship in the range of 10 μM to 100 μM with a detection limit of 4 μM, as illustrated in Figure 13b. Figure 14b draws the calibration curve for H_2O_2 with a linear range from 10 to 250 μM for the TMB–H_2O_2–2D CTAB-MoSe$_2$ system. The detection limit was also reckoned to be around 4 μM. It shows that the TMB–H_2O_2–2D CTAB-MoSe$_2$ system could have a wider linear range compared with that of the TMB–H_2O_2–MoSe$_2$ QDs system. Finally, we compare some representative colorimetric detections of H_2O_2 by using novel 2D materials in Table 1 [69–72]. It can be seen that the colorimetric sensing ability of H_2O_2 based on the peroxidase-like property of our MoSe$_2$-based catalyst is comparable to other reported 2D materials-based colorimetric platforms. Therefore, our work provides a facile, simple, cost-effective, and alternative 2D materials-based colorimetric sensing platform for sensitive detection of H_2O_2. In principle, this sensing platform can be applied to a few diverse applications, yet proper selectivity tests should then be imposed to understand the specific accuracy in the measurement [31,73–75].
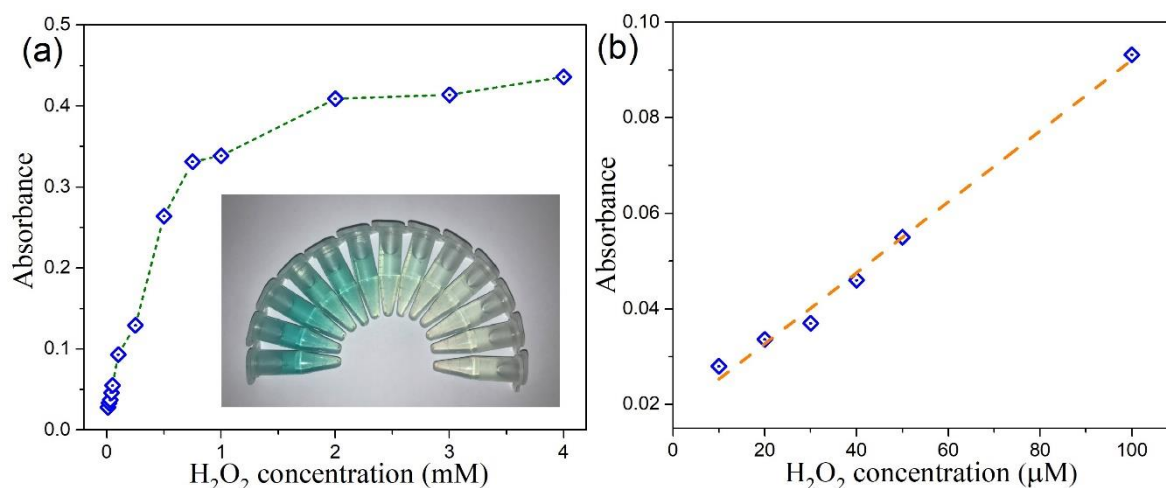
Figure 13. (**a**) The absorbance changes at 652 nm for MoSe$_2$ QDs in different amount of H$_2$O$_2$ (0.01, 0.02, 0.03, 0.04, 0.05, 0.1, 0.25, 0.5, 0.75, 1, 2, 3 and 4 mM). Inset: the images of color contrast for different concentrations of H$_2$O$_2$. (**b**) The linear calibration plot for H$_2$O$_2$.
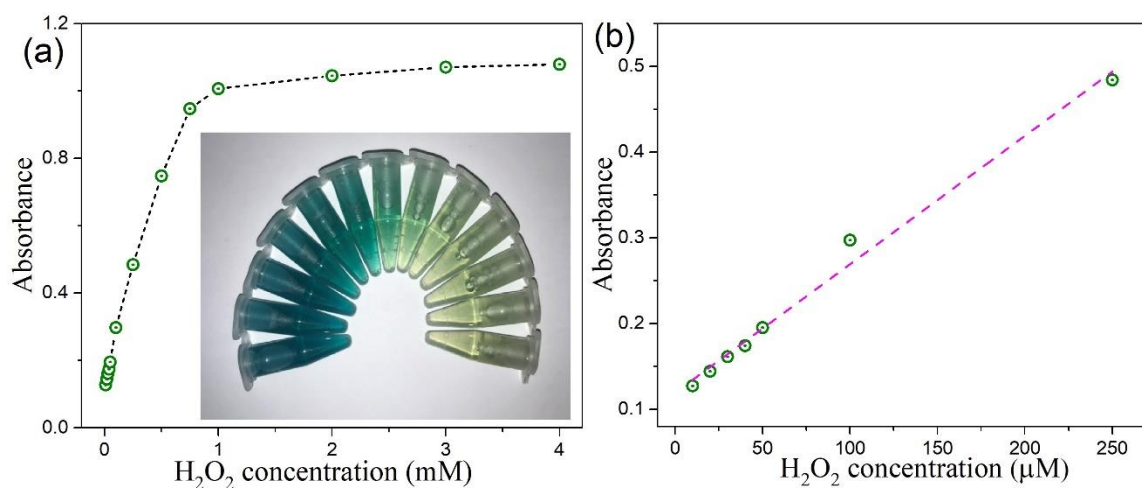

Figure 14. (**a**) The dose-response curve for H$_2$O$_2$ detection by using 2D CTAB-MoSe$_2$ NSs as artificial enzyme. The inset are the photos of reaction solutions after adding different concentrations of H$_2$O$_2$. (**b**) The linear calibration plot for H$_2$O$_2$ concentration.

Table 1. Comparison of colorimetric detections of H$_2$O$_2$ in the linear range and detection limit between our MoSe$_2$ nanostructures and other peroxidase mimics based on nanoscale 2D materials.

Catalyst	Linear Range (μM)	Detection Limit (μM)	Ref.
Positively-charged Au nanoparticles (NPs)h-BN/N-MoS$_2$	2–200	0.5	[15]
h-BN/N-MoS$_2$	1–1000	0.4	[69]
Few-layered MoSe$_2$ nanosheets (NSs)	10–160	0.4	[27]
MoS$_2$ NPs	3–120	1.25	[23]
SDS–MoS$_2$ NPs	2–100	0.32	[24]
g-C$_3$N$_4$	5–100	1	[70]
MoS$_2$ QDs/g-C$_3$N$_4$ NSs	2–50	0.155	[71]
WS$_2$ Nanosheets	5–200	1.5	[72]
2D CTAB-MoSe$_2$	10–250	4	This work
0D MoSe$_2$ QDs quantum dots (QDs)	10–100	4	This work

4. Conclusions

In summary, we prepared 2D and 0D $MoSe_2$ nanostructures based on systematic and non-toxic top-down strategies. The characteristic excitation-dependent PL of the $MoSe_2$ QDs can be attributed to the polydispersity of the synthesized QDs. The Raman shift of ultrathin $MoSe_2$ nanosheets manifests the 2D nature of its structure. We demonstrated that these $MoSe_2$ nanostructures possess intrinsic peroxidase-like activity in that they can facilitate the oxidation of TMB in the presence of H_2O_2, generating a visible color reaction. For the catalysis mechanism, kinetic analysis indicates that the catalytic reaction follows the typical Michaelis–Menten theory and a ping–pong mechanism. Moreover, active species study shows that $\dot{O}_2^-$ plays a pivotal role in the peroxidase-like catalytic reaction. Based on the color reaction of TMB catalyzed by our $MoSe_2$ nanomaterials, we have developed a new colorimetric method for H_2O_2 detection by using 2D and 0D $MoSe_2$ nanostructures as peroxidase mimetics. It is shown that the colorimetric sensing capability of our $MoSe_2$ catalysts is comparable to other 2D materials-based colorimetric platforms. Overall, the synthesis strategy we proposed is environmentally friendly and economic, and it can easily be adapted to construct novel inorganic low-dimensional enzyme-free mimetic with intrinsic catalytic activity. The potential of the presented 2D and 0D $MoSe_2$ nanostructures for use as a catalyst in other oxidation reactions could be explored in the extended study and this could create a new opportunity for this enzyme-mimicking $MoSe_2$ nanostructures in many significant fields, such as environmental protection, food monitoring, medical diagnostics, and photocatalysis.

Supplementary Materials: The following are available online at http://www.mdpi.com/2079-4991/10/10/2045/s1, Figure S1: UV–vis absorption spectra of $MoSe_2$ QDs with different concentrations of H_2O_2, Figure S2: UV–vis absorption spectra of 2D CTAB-$MoSe_2$ NSs with different amounts of H_2O_2, Table S1: Michaelis–Menten parameters of the 2D CTAB-$MoSe_2$ NSs and 0D $MoSe_2$ QDs.

Author Contributions: Conceptualization, D.-R.H. and Y.-Q.P.; methodology, Y.-Q.P. and K.H.S.; validation, Y.-Q.P., K.H.S. and S.E.I.; formal analysis, Y.-Q.P. and K.H.S.; investigation, Y.-Q.P. and K.H.S.; data curation, D.-R.H. and Y.-Q.P.; writing—original draft preparation, D.-R.H. and Y.-Q.P.; writing—review and editing, D.-R.H. and C.-T.L.; resources, H.-F.W. and M.M.C.C.; supervision, D.-R.H.; project administration, D.-R.H.; funding acquisition, D.-R.H. and C.-T.L. All authors have read and agreed to the published version of the manuscript.

Conflicts of Interest: The authors declare no conflict of interest.

References

1. Zhu, J.; Wang, S. In situ growth of copper oxide-graphite carbon nitride nanocomposites with peroxidase-mimicking activity for electrocatalytic and colorimetric detection of hydrogen peroxide. *Carbon* **2018**, *129*, 29–37. [CrossRef]

2. Mao, L.; Osborne, P.G.; Yamamoto, K.; Kato, T. Continuous on-line measurement of cerebral hydrogen peroxide using enzyme-modified ring–disk plastic carbon film electrode. *Anal Chem.* **2002**, *74*, 3684–3689. [CrossRef] [PubMed]

3. Belousov, V.V.; Fradkov, A.F.; Lukyanov, K.A.; Staroverov, D.B.; Shakhbazov, K.S.; Terskikh, A.V.; Lukyanov, S. Genetically encoded fluorescent indicator for intracellular hydrogen peroxide. *Nat. Methods* **2006**, *3*, 281–286. [CrossRef] [PubMed]

4. Xu, M.; Han, J.-M.; Zhang, Y.; Yang, X.; Zang, L. A selective fluorescence turn-on sensor for trace vapor detection of hydrogen peroxide. *Chem. Commun.* **2013**, *49*, 11779–11781. [CrossRef]

5. Srikun, D.; Albers, A.E.; Nam, C.I.; Iavaron, A.T.; Chang, C.J.J. Organelle-targetable fluorescent probes for imaging hydrogen peroxide in living cells via SNAP-Tag protein labeling. *J. Am. Chem. Soc.* **2010**, *132*, 4455–4465. [CrossRef]

6. Xu, J.; Shang, F.J.; Luong, J.H.T.; Razeeb, K.M.; Glennon, J.D. Direct electrochemistry of horseradish peroxidase immobilized on a monolayer modified nanowire array electrode. *Biosens. Bioelectron.* **2010**, *25*, 1313–1318. [CrossRef]

7. Ding, J.W.; Zhang, K.; Wei, G.; Su, Z.Q. Fabrication of polypyrrole nanoplates decorated with silver and gold nanoparticles for sensor applications. *RSC Adv.* **2015**, *5*, 69745–69752. [CrossRef]

8. Wei, H.; Wang, E.K. Fe_3O_4 magnetic nanoparticles as peroxidase mimetics and their applications in H_2O_2 and glucose detection. *Anal. Chem.* **2008**, *80*, 2250–2254. [CrossRef]

9. Bao, Y.-W.; Hua, X.-W.; Ran, H.-H.; Zeng, J.; Wu, F.-G. Metal-doped carbon nanoparticles with intrinsic peroxidase-like activity for colorimetric detection of H_2O_2 and glucose. *J. Mater. Chem. B* **2019**, *7*, 296–304. [CrossRef]

10. Nerthigan, Y.; Sharma, A.K.; Pandey, S.; Sharma, K.H.; Khan, M.S.; Hang, D.-R.; Wu, H.-F. Glucose oxidase assisted visual detection of glucose using oxygen deficient α-MoO_{3-x} nanoflakes. *Microchim. Acta* **2018**, *185*, 65. [CrossRef]

11. Sharma, A.K.; Pandey, S.; Sharma, K.H.; Nerthigan, Y.; Khan, M.S.; Hang, D.-R.; Wu, H.-F. Two dimensional α-MoO_{3-x} nanoflakes as bare eye probe for hydrogen peroxide in biological fluids. *Anal. Chim. Acta* **2018**, *1015*, 58–65. [CrossRef] [PubMed]

12. Tang, X.Q.; Zhang, Y.D.; Jiang, Z.W.; Wang, D.M.; Huang, C.Z.; Li, Y.F. Fe_3O_4 and metal–organic framework MIL-101(Fe) composites catalyze luminol chemiluminescence for sensitively sensing hydrogen peroxide and glucose. *Talanta* **2018**, *179*, 43–50. [CrossRef]

13. Jin, L.; Meng, Z.; Zhang, Y.; Cai, S.; Zhang, Z.; Li, C.; Shang, L.; Shen, Y. Ultrasmall Pt nanoclusters as robust peroxidase mimics for colorimetric detection of glucose in human serum. *ACS Appl. Mater. Interfaces* **2017**, *9*, 10027–10033. [CrossRef]

14. Wang, S.; Sun, J.; Jia, Y.; Yang, L.; Wang, N.; Xianyu, Y.; Chen, W.; Li, X.; Cha, R.; Jiang, X. Nanocrystalline cellulose-assisted generation of silver nanoparticles for nonenzymatic glucose detection and antibacterial agent. *Biomacromolecules* **2016**, *17*, 2472–2478. [CrossRef]

15. Jv, Y.; Li, B.X.; Cao, R. Positively-charged gold nanoparticles as peroxidiase mimic and their application in hydrogen peroxide and glucose detection. *Chem. Commun.* **2010**, *46*, 8017–8019. [CrossRef] [PubMed]

16. Teo, W.Z.; Chng, E.L.K.; Sofer, Z.; Pumera, M. Cytotoxicity of exfoliated transition-metal dichalcogenides (MoS_2, WS_2, and WSe_2) is lower than that of graphene and its analogues. *Chem. Eur. J.* **2014**, *20*, 9627–9632. [CrossRef]

17. Sorkin, V.; Pan, H.; Shi, H.; Quek, S.Y.; Zhang, Y.W. Nanoscale transition metal dichalcogenides: Structures, properties, and applications. *Crit. Rev. Solid State Mater. Sci.* **2014**, *39*, 319–367. [CrossRef]

18. Singh, A.K.; Hwang, C.; Eom, J. Low-Voltage and high-performance multilayer MoS_2 field-effect transistors with graphene electrodes. *ACS Appl. Mater. Interfaces* **2016**, *8*, 34699–34705. [CrossRef]

19. Joseph, N.; Muhammed Shafi, P.; Chandra Bose, A. Recent advances in 2D-MoS_2 and its composite nanostructures for supercapacitor electrode application. *Energy Fuels* **2020**, *34*, 6558–6597. [CrossRef]

20. Lin, X.; Wang, X.; Zhou, Q.; Wen, C.; Su, S.; Xiang, J.; Cheng, P.; Hu, X.; Li, Y.; Wang, X.; et al. Magnetically recyclable MoS_2/Fe_3O_4 hybrid composite as visible light responsive photocatalyst with enhanced photocatalytic performance. *ACS Sustain. Chem. Eng.* **2018**, *7*, 1673–1682. [CrossRef]

21. Kalantar-zadeh, K.; Ou, J.Z. Biosensors based on two-dimensional MoS_2. *ACS Sens.* **2016**, *1*, 5–16. [CrossRef]

22. Gan, X.; Zhao, H.; Quan, X. Two-dimensional MoS_2: A promising building block for biosensors. *Biosens. Bioelectron.* **2017**, *89*, 56–71. [CrossRef] [PubMed]

23. Zhao, Y.; Huang, Y.; Wu, J.; Zhan, X.; Xie, Y.; Tang, D.; Cao, H.; Yun, W. Mixed-solvent liquid exfoliated MoS_2 NPs as peroxidase mimetics for colorimetric detection of H_2O_2 and glucose. *RSC Adv.* **2018**, *8*, 7252–7259. [CrossRef]

24. Zhao, K.; Gu, W.; Zheng, S.S.; Zhang, C.L.; Xian, Y.Z. SDS-MoS_2 nanoparticles as highly-efficient peroxidase mimetics for colorimetric detection of H_2O_2 and glucose. *Talanta* **2015**, *141*, 47–52. [CrossRef] [PubMed]

25. Choi, S.Y.; Kim, Y.; Chung, H.S.; Kim, A.R.; Kwon, J.D.; Park, J.; Kim, Y.L.; Kwon, S.H.; Hahm, M.G.; Cho, B. Effect of Nb doping on chemical sensing performance of two-dimensional layered $MoSe_2$. *ACS Appl. Mater. Interfaces* **2017**, *9*, 3817–3823. [CrossRef]

26. Gholamvand, G.; McAteer, D.; Backes, C.; McEvoy, N.; Harvey, A.; Berner, N.C.; Hanlon, D.; Bradley, C.; Godwin, I.; Rovetta, A.; et al. Comparison of liquid exfoliated transition metal dichalcogenides reveals $MoSe_2$ to be the most effective hydrogen evolution catalyst. *Nanoscale* **2016**, *8*, 5737–5749. [CrossRef]

27. Wu, X.; Chen, T.; Wang, J.; Yang, G. Few-layered MoSe$_2$ nanosheets as an efficient peroxidase nanozyme for highly sensitive colorimetric detection of H$_2$O$_2$ and xanthine. *J. Mater. Chem. B* **2018**, *6*, 105–111. [CrossRef]

28. Pan, J.; Zhu, X.; Chen, X.; Zhao, Y.; Liu, J. Gd^{3+}-doped MoSe$_2$ nanosheets used as a theranostic agent for bimodal imaging and highly efficient photothermal cancer therapy. *Biomater. Sci.* **2018**, *6*, 372–387. [CrossRef]

29. Li, B.L.; Setyawati, M.I.; Zou, H.L.; Dong, J.X.; Luo, H.Q.; Li, N.B.; Leong, D.T. Emerging 0D transition-metal dichalcogenides for sensors, biomedicine, and clean energy. *Small* **2017**, *13*, 1700527. [CrossRef]

30. Xu, Y.; Wang, X.; Zhang, W.L.; Lv, F.; Guo, S. Recent progress in two-dimensional inorganic quantum dots. *Chem. Soc. Rev.* **2018**, *47*, 586–625. [CrossRef]

31. Wang, X.; Wu, Q.; Jiang, K.; Wang, C.; Zhang, C. One-step synthesis of water-soluble and highly fluorescent MoS$_2$ quantum dots for detection of hydrogen peroxide and glucose. *Sens. Actuators B* **2017**, *252*, 183–190. [CrossRef]

32. Hang, D.-R.; Sun, D.-Y.; Chen, C.-H.; Wu, H.-F.; Chou, M.M.C.; Islam, S.E.; Sharma, K.H. Facile bottom-up preparation of WS$_2$-based water-soluble quantum dots as luminescent probes for hydrogen peroxide and glucose. *Nanoscale Res. Lett.* **2019**, *14*, 271. [CrossRef] [PubMed]

33. Gerislioglu, B.; Dong, L.; Ahmadivand, A.; Hu, H.; Nordlander, P.; Halas, N.J. Monolithic metal dimer-on-film structure: New plasmonic properties introduced by the underlying metal. *Nano Lett.* **2020**, *20*, 2087–2093. [CrossRef]

34. Ahmadivand, A.; Gerislioglu, B. Tunable plexciton dynamics in electrically biased nanojunctions. *J. Appl. Phys.* **2020**, *128*, 063101. [CrossRef]

35. Gerislioglu, B.; Ahmadivand, A. Theoretical study of photoluminescence spectroscopy of strong exciton-polariton coupling in dielectric nanodisks with anapole states. *Mater. Today Chem.* **2020**, *16*, 100254. [CrossRef]

36. Backes, C.; Higgins, T.M.; Kelly, A.; Boland, C.; Harvey, A.; Hanlon, D.; Coleman, J.N. Guidelines for exfoliation, characterization and processing of layered materials produced by liquid exfoliation. *Chem. Mater.* **2017**, *29*, 243–255. [CrossRef]

37. Hang, D.-R.; Sharma, K.H.; Chen, C.-H.; Islam, S.E. Enhanced photocatalytic performance of ZnO nanorods coupled by two-dimensional α-MoO$_3$ nanoflakes under UV and visible light irradiation. *Chem. Eur. J.* **2016**, *22*, 12777–12784. [CrossRef]

38. Chhetri, S.; Adak, N.C.; Samanta, P.; Murmu, N.C.; Kuila, T. Exploration of mechanical and thermal properties of CTAB-modified MoS$_2$/LLDPE composites prepared by melt mixing. *J. Compos. Sci.* **2018**, *2*, 37. [CrossRef]

39. Hang, D.-R.; Sharma, K.H.; Islam, S.E.; Chen, C.; Chou, M.M.C. Resonant Raman scattering and photoluminescent properties of nonpolar *a*-plane ZnO thin film on LiGaO$_2$ substrate. *Appl. Phys. Express* **2014**, *7*, 041101. [CrossRef]

40. Zhu, C.; Huang, Y.; Xu, F.; Gao, P.; Ge, B.; Chen, J.; Zeng, H.; Sutter, E.; Sutter, P.; Sun, L. Defect-laden MoSe$_2$ quantum dots made by turbulent shear mixing as enhanced electrocatalysts. *Small* **2017**, *13*, 1700565. [CrossRef]

41. Islam, S.E.; Hang, D.-R.; Chen, C.-H.; Sharma, K.H. Facile and cost-efficient synthesis of quasi-0D/2D ZnO/MoS$_2$ nanocomposites for highly enhanced visible-light-driven photocatalytic degradation of organic pollutants and antibiotics. *Chem. Eur. J.* **2018**, *24*, 9305–9315. [CrossRef]

42. Qu, B.; Yu, X.; Chen, Y.; Zhu, C.; Li, C.; Yin, Z.; Zhang, X. Ultrathin MoSe$_2$ nanosheets decorated on carbon fiber cloth as binder-free and high-performance electrocatalyst for hydrogen evolution. *ACS Appl. Mater. Interfaces* **2015**, *7*, 14170–14715. [CrossRef]

43. Koroteev, V.; Bulusheva, L.; Asanov, I.; Shlyakhova, E.; Vyalikh, D.; Okotrub, A. Charge transfer in the MoS$_2$/carbon nanotube composite. *J. Phys. Chem. C* **2011**, *115*, 21199–21204. [CrossRef]

44. Guo, X.; Cao, G.; Ding, F.; Li, X.; Zhen, S.; Xue, Y.; Yan, Y.; Liu, T.; Sun, K. A bulky and flexible electrocatalyst for efficient hydrogen evolution based on the growth of MoS$_2$ nanoparticles on carbon nanofiber foam. *J. Mater. Chem. A* **2015**, *3*, 5041–5046. [CrossRef]

45. Smith, R.J.; King, P.J.; Lotya, M.; Wirtz, C.; Khan, U.; De, S.; O'Neill, A.; Duesberg, G.S.; Grunlan, J.C.; Moriarty, G. Large-scale exfoliation of inorganic layered compounds in aqueous surfactant solutions. *Adv. Mater.* **2011**, *23*, 3944–3948. [CrossRef] [PubMed]

46. Wang, K.; Feng, Y.; Chang, C.; Zhan, J.; Wang, C.; Zhao, Q.; Colemon, J.N.; Zhang, L.; Blau, W.J.; Wang, J. Broadband ultrafast nonlinear absorption and nonlinear refraction of layered molybdenum dichalcogenide semiconductors. *Nanoscale* **2014**, *6*, 10530–10535. [CrossRef]

47. Dong, N.; Li, Y.; Feng, Y.; Zhang, S.; Zhang, X.; Chang, C.; Fan, J.; Zhang, L.; Wang, J. Optical limiting and theoretical modelling of layered transition metal dichalcogenide nanosheets. *Sci. Rep.* **2015**, *5*, 14646. [CrossRef]

48. Wang, G.; Gerber, I.C.; Bouet, L.; Lagarde, D.; Balocchi, A.; Vidal, M.; Amand, T.; Marie, X.; Urbaszek, B. 2015 Exciton states in monolayer MoSe$_2$: Impact on interband transitions. *2D Mater.* **2015**, *2*, 045005. [CrossRef]

49. Roy, S.; Neupane, G.P.; Dhakal, K.P.; Lee, J.; Yun, S.J.; Han, G.H.; Kim, J. Observation of charge transfer in heterostructures composed of MoSe$_2$ quantum dots and a monolayer of MoS$_2$ or WSe$_2$. *J. Phys. Chem. C* **2017**, *121*, 1997–2004. [CrossRef]

50. Xu, S.; Li, D.; Wu, P. One-pot, facile, and versatile synthesis of monolayer MoS$_2$/WS$_2$ quantum dots as bioimaging probes and efficient electrocatalysts for hydrogen evolution reaction. *Adv. Funct. Mater.* **2015**, *25*, 1127–1136. [CrossRef]

51. Yan, Y.; Zhang, C.; Gu, W.; Ding, C.; Li, X.; Xian, Y. Facile synthesis of water-soluble WS$_2$ quantum dots for turn-on fluorescent measurement of lipoic acid. *J. Phys. Chem. C* **2016**, *120*, 12170–12177. [CrossRef]

52. Hang, D.-R.; Islam, S.E.; Sharma, K.H.; Chen, C.; Liang, C.-T.; Chou, M.M.C. Optical characteristics of nonpolar *a*-plane ZnO thin film on (010) LiGaO$_2$ substrate. *Semicond. Sci. Technol.* **2014**, *29*, 085004. [CrossRef]

53. Hang, D.-R.; Islam, S.E.; Chen, C.-H.; Sharma, K.H. Full solution-processed synthesis and mechanisms of a recyclable and bifunctional Au/ZnO plasmonic platform for enhanced UV/Vis photocatalysis and optical properties. *Chem. Eur. J.* **2016**, *22*, 14950–14961. [CrossRef]

54. Gan, Z.X.; Liu, L.Z.; Wu, H.Y.; Hao, Y.L.; Shan, Y.; Wu, X.L.; Chu, P.K. Quantum confinement effects across two-dimensional planes in MoS$_2$ quantum dots. *Appl. Phys. Lett.* **2015**, *106*, 233113. [CrossRef]

55. Roy, A.; Movva, H.C.P.; Satpati, B.; Kim, K.; Dey, R.; Rai, A.; Pramanik, T.; Guchhait, S.; Tutuc, E.; Banerjee, S.K. Structural and electrical properties of MoTe$_2$ and MoSe$_2$ grown by molecular beam epitaxy. *ACS Appl. Mater. Interfaces* **2016**, *8*, 7396–7402. [CrossRef]

56. Lee, C.; Yan, H.; Brus, L.E.; Heinz, T.F.; Hone, J.; Ryu, S. Anomalous lattice vibrations of single- and few-layer MoS$_2$. *ACS Nano* **2010**, *4*, 2695–2700. [CrossRef] [PubMed]

57. Tonndorf, P.; Schmidt, R.; Böttger, P.; Zhang, X.; Börner, J.; Liebig, A.; Albrecht, M.; Kloc, C.; Gordan, O.; Zahn, D.R.T.; et al. Photoluminescence emission and Raman response of monolayer MoS$_2$, MoSe$_2$, and WSe$_2$. *Opt. Express* **2013**, *21*, 4908. [CrossRef] [PubMed]

58. Chen, S.Y.; Zheng, C.; Fuhrer, M.S.; Yan, J. Helicity-resolved Raman scattering of MoS$_2$, MoSe$_2$, WS$_2$, and WSe$_2$ atomic layers. *Nano Lett.* **2015**, *15*, 2526–2532. [CrossRef]

59. Luo, X.; Zhao, Y.; Zhang, J.; Xiong, Q.; Quek, S.Y. Anomalous frequency trends in MoS$_2$ thin films attributed to surface effects. *Phys. Rev. B* **2013**, *88*, 075320. [CrossRef]

60. Kim, K.; Lee, J.U.; Nam, D.Y.; Cheong, H. Davydov splitting and excitonic resonance effects in Raman spectra of few-layer MoSe$_2$. *ACS Nano* **2016**, *10*, 8113–8120. [CrossRef]

61. Luan, C.-Y.; Xie, S.; Ma, C.; Wang, S.; Kong, Y.; Xu, M. Elucidation of luminescent mechanisms of size-controllable MoSe$_2$ quantum dots. *Appl. Phys. Lett.* **2017**, *111*, 073105. [CrossRef]

62. Qiao, F.M.; Qi, Q.Q.; Wang, Z.Z.; Xu, K.; Ai, S.Y. MnSe-loaded g-C$_3$N$_4$ nanocomposite with synergistic peroxidase-like catalysis: Synthesis and application toward colorimetric biosensing of H$_2$O$_2$ and glucose. *Sensor. Actuator. B Chem.* **2016**, *229*, 379–386. [CrossRef]

63. Chen, L.J.; Sun, B.; Wang, X.; Qiao, F.M.; Ai, S.Y. 2D ultrathin nanosheets of Co-Al layered double hydroxides prepared in L-asparagine solution enhanced peroxidase-like activity and colorimetric detection of glucose. *J. Mater. Chem. B* **2013**, *1*, 2268–2274. [CrossRef] [PubMed]

64. Gao, L.; Zhuang, J.; Nie, L.; Zhang, J.; Zhang, Y.; Gu, N.; Wang, T.; Feng, J.; Yang, D.; Perrett, S.; et al. Intrinsic peroxidase-like activity of ferromagnetic nanoparticles. *Nat. Nanotechnol.* **2007**, *2*, 577–583. [CrossRef]

65. Qiao, F.M.; Chen, L.J.; Li, X.; Li, L.; Ai, S.Y. Peroxidase-like activity of manganese selenide nanoparticles and its analytical application for visual detection of hydrogen peroxide and glucose. *Sen. Actuator B Chem.* **2014**, *193*, 255–262. [CrossRef]

66. Peng, J.; Weng, J. Enhanced peroxidase-like activity of MoS$_2$/graphene oxide hybrid with light irradiation for glucose detection. *Biosens. Bioelectron.* **2017**, *89*, 652–658. [CrossRef]

67. Vinita, N.R.N.; Prakash, R. One step synthesis of AuNPs@MoS$_2$-QDs composite as a robust peroxidase-mimetic for instant unaided eye detection of glucose in serum, saliva and tear. *Sen. Actuator B Chem.* **2018**, *263*, 109–119. [CrossRef]

68. Ju, P.; Xiang, Y.H.; Xiang, Z.B.; Wang, M.; Zhao, Y.; Zhang, D.; Yu, J.Q.; Han, X.X. BiOI hierarchical nanoflowers as novel robust peroxidase mimetics for colorimetric detection of H_2O_2. *RSC Adv.* **2016**, *6*, 17483–17493. [CrossRef]

69. Zhang, X.; Gao, Y.F. 2D/2D h-BN/N-doped MoS_2 heterostructure catalyst with enhanced peroxidase-like performance for visual colorimetric determination of H_2O_2. *Chem. Asian J.* **2020**, *15*, 1315–1323. [CrossRef]

70. Lin, T.R.; Zhong, L.S.; Wang, J.; Guo, L.Q.; Wu, H.Y.; Guo, Q.Q.; Fu, F.F.; Chen, G.N. Graphite-like carbon nitrides as peroxidase mimetics and their applications to glucose detection. *Biosens. Bioelectron.* **2014**, *59*, 89–93. [CrossRef]

71. Ju, P.; He, Y.; Wang, M.; Han, X.; Jiang, F.; Sun, C.; Wu, C. Enhanced Peroxidase-like activity of MoS_2 quantum dots functionalized g-C_3N_4 nanosheets towards colorimetric detection of H_2O_2. *Nanomaterials* **2018**, *8*, 976. [CrossRef] [PubMed]

72. Chen, Q.; Chen, J.; Gao, C.J.; Zhang, M.L.; Chen, J.Y.; Qiu, H.D. Hemin-functionalized WS_2 nanosheets as highly active peroxidase mimetics for label-free colorimetric detection of H_2O_2 and glucose. *Analyst* **2015**, *140*, 2857–2863. [CrossRef] [PubMed]

73. Ma, J.; Yu, H.; Jiang, X.; Luo, Z.; Zheng, Y. High sensitivity label-free detection of Fe^{3+} ion in aqueous solution using fluorescent MoS_2 quantum dots. *Sens. Actuators B* **2019**, *281*, 989–997. [CrossRef]

74. Chen, J.; Li, Y.; Lv, K.; Zhong, W.; Wang, H.; Wu, Z.; Yi, P.; Jiang, J. Cyclam-functionalized carbon dots sensor for sensitive and selective detection of copper(II) ion and sulfide anion in aqueous media and its imaging in live cells. *Sens. Actuators B* **2016**, *224*, 298–306. [CrossRef]

75. Chhetri, R.K.; Kaarsholm, K.M.S.; Andersen, H.R. Colorimetric quantification methods for peracetic acid together with hydrogen peroxide for water disinfection process control. *Int. J. Environ. Res. Public Health* **2020**, *17*, 4656. [CrossRef] [PubMed]

Publisher's Note: MDPI stays neutral with regard to jurisdictional claims in published maps and institutional affiliations.